# RSC Advances

ROYAL SOCIETY
OF **CHEMISTRY**

www.rsc.org/advances

# Journal Name

## COMMUNICATION

# Perylene Bisimide as the Cathode Modifier in Organic Photovoltaics: The Role of Aggregation Morphology on the Interlayer Performance

Wenqiang Zhang,[a,c] Shu Zhong,[b] Li Nian,[a] Yulan Chen,[a] Zengqi Xie,*[a] Linlin Liu,[a] Muddasir Hanif,[a] Wei Chen*[b] and Yuguang Ma[a]

**Nanorods and nanoparticles of perylene bisimides (PBI-1) were prepared and applied as cathode interlayer in organic photovoltaic devices. The device performance showed important relation with the morphology of the interlayer.**

Organic photovoltaics (OPVs) are important for their advantages such as light weight, low cost and flexibility [1-4]. In conventional OPVs, the indium-tin oxide (ITO) anode is usually modified with an acidic composite polyelectrolyte, namely poly(3,4-ethylene-dioxythiophene):poly(styrene sulfonate) (PEDOT:PSS) (that may corrode ITO slowly),[5-10] but pH-neutral conjugated polyelectrolytes are preferred.[11-15] The cathode side of OPV may contain alkali metals like easy to oxidize calcium and barium. As a counterpart, inverted OPVs possess advantage of higher stability due to the non-usage of acidic PEDOT:PSS and the replacement of alkali metals by the air stable metals [16-18]. The ITO work function needs modulation to adapt energy level alignment between the electrode and the active layer (through surface modification) by the interlayer materials. Recently, surfactants like poly[(9,9-bis(3-(N,N-dimethyl-amino) propyl)-2,7-fluorene)-alt-2,7-(9,9–dioctylfluorene)] (PFN) and non-conjugated polyethyl-enimine ethoxylated (PEIE) have been used to significantly decrease the ITO work function and thus resulting in highly efficient inverted OPVs [19, 20]. Beside these, some interesting biomaterials such as amino acids, peptides and zwitterion molecules were also reported as ITO modifiers for the construction of the inverted OPVs [21-24]. Typically the thickness of the interlayer is less than 10 nm for the low conductivity of such materials, and ITO surface need to be covered uniformly to avoid the leak current. The difficult fabrication procedure of an interlayer may restrict its wide application especially in the printed electronics for future applications. To realize massive production of OPVs, nowadays more and more attention has been paid on the development of highly conductive and thickness insensitive interlayer materials [25, 26].

Perylene bisimides (PBIs) are a class of archetype, high electron mobility, n-type organic semiconductors [27]. Most recently, several research groups including ours have reported the application of PBIs as

the cathode interlayer for electron extraction from the active layer in the inverted OPVs [28-31]. These researchers showed that the work function of ITO decreases to different extents after coated with a thin layer of PBI. It is well known that work function is the minimum energy needed to move an electron from the Fermi level into vacuum, which is a property of the surface depending on many factors such as crystal face, molecular orientation, morphology and others[32]. However, the difficult morphology control during the solution processing of the classical interlayer materials, the influence of the interlayer morphology on the work function requires deeper understanding. PBIs usually have strong tendency to form supramolecular aggregates possessing ordered molecular stacking, which benefits the thick interlayer because of the possible enhanced electron mobility. Further, the morphology of the supramolecular aggregates can be easily controlled through tuning the intermolecular interactions, which facilitates the study of the morphological dependence of the interlayer performance on the morphology [33]. In this contribution, we report the precise control of the aggregation morphology of PBI-1 (Fig. 1a) and the application of the different morphological aggregates as cathode interlayer in the inverted photovoltaic devices. Our results indicate that the charge transfer properties between $C_{60}$ and the cathode strongly correlate with the aggregation morphologies of the PBI-1 interlayer, which gives different device performances.

PBI dyes are typically insoluble owing to the strong π-π stacking between the adjacent molecules [27]. Recently, a solvent-selective soluble PBI-1 bearing two NH groups on imide positions has been reported (Fig. 1a) [34], which forms strong intermolecular multiple hydrogen bonds (N-H---O) in the nonpolar solvents (Fig. 1b). The hydrogen bonds lead to one-dimensional linear growth of the aggregates with the aid of the intermolecular π-π stacking interaction (Fig. 1c). The diameter of these nanofibers can be accurately controlled (30 nm) via regulating the concentrations of the solution in chloroform and the revolving speed of spin-coater. In principle, the morphology and dimensions of the nanostructures could be accurately controlled by partially destroying the hydrogen bonds. We successfully obtained rod
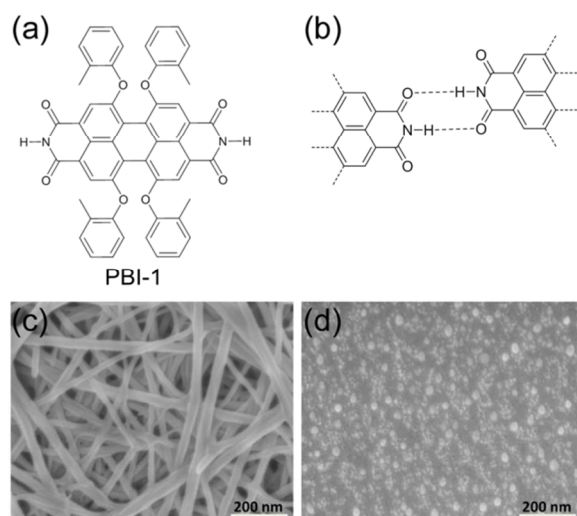
Figure 1. (a) Chemical structure of PBI-1. (b) Schematics of intermolecular hydrogen bonds of two adjacent PBI-1 molecules. (c, d) SEM images of PBI-1 nanofibers and nanoparticles on glass substrates via spin-coating from CHCl₃ solution (c) and THF solution (d) of PBI-1, respectively. The concentrations for both were 1 mg/mL, and the revolving speed was 3000 r/min.



Figure 2. UV/vis spectra of PBI-1 solutions and aggregates. The nanoparticles and nanofibers were prepared via spin-coating method on glass substrates from THF solution (1 mg/mL) and CHCl₃ solution (1 mg/mL), respectively.

and particle-like aggregates by spin-coating the PBI-1 chloroform solutions by adding small amount of acetic acid as additives (for details see SEI). Here the acetic acid molecule acts as the aggregation inhibitor because the much stronger hydrogen bonds may form between PBI-1 molecules and the acid molecules. The controllable aggregation allowed investigation of morphology on the physical properties when using the aggregates as the electrode modifier as discussed below.

Indeed, it is more convenient to control the morphology of the aggregates by changing the organic solvents. In aprotic solvents such as chloroform, this PBI-1 can form one dimensional nanofiber (Fig. 1c). Interestingly, the hydrogen bond interaction can be inhibited in some solvents like tetrahydrofuran (THF) likely due to the solute-solvent (NH…O) interactions between (PBI-1)-THF or the effect from the residual $H_2O$ in THF similar to the acetic acid. The inhibited intermolecular hydrogen bonding between PBI-1 molecules is directly reflected by the increase of solubility; that is the solubility of this PBI-1 in THF is >10 mg/mL, which is larger than the solubility in chloroform (~5 mg/mL) and toluene (~$10^{-2}$ mg/mL) at room temperature). We used 1 mg/mL THF solution to form particle-like aggregates on the ITO glass substrate by spin-coating method (Fig. 1d). The size of the nanoparticles is about several nanometers to 30 nm. Although the aggregation morphology obtained from chloroform and THF solutions is quite different, the molecular stacking mode is similar based on the evolution of the electronic absorption spectra from molecules to aggregates (Fig. 2). For both cases, the absorption of the aggregates shows very large bathochromic shifts of (70~80 nm) compared with those in solutions, which indicates J-aggregation [35]. The fibroid aggregates show bathochromic shifts of 9 nm compared with that of the particle-like aggregates, which indicates the fibroid aggregates possess more ordered molecular stacking. The aggregation model of PBI-1 (intermolecular multiple hydrogen bonds help formation of J-aggregates) and the UV-vis absorption spectra, indicate that the fibroid aggregates may possess long distance molecular orientation along the
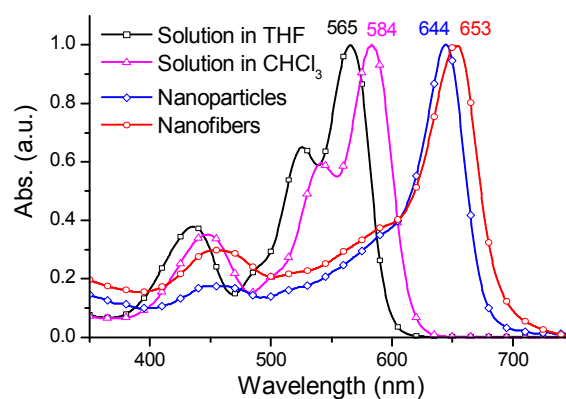
long axis direction of the fibers. While the particles may just show local ordered molecular stacking within distance of several molecules. This means the molecular long axis (N-N direction) is parallel to the substrate in the fibrous aggregates on the glass substrate, but it is disordered for the particle-like samples. Here, we report modification of ITO surface by the *in situ* formed nano-aggregates of PBI-1, and their different morphology effects on the electronic properties of ITO electrode by UPS measurements [36-38]. The nanofibers and nanoparticles of PBI-1 on ITO surface were obtained via spin-coating from chloroform and THF solutions respectively. To minimize the effect of film thickness on the electronic properties, the thickness of the PBI-1 on ITO was kept 10 nm by control over the solution concentration and revolving speed of the spin-coater, as discussed below. The work functions of the ITO covered with PBI-1 nanofibers and nanoparticles were determined to be 3.50 eV and 3.79 eV, which is much lower (1.07 eV and 0.78 eV) when compared with 4.57 eV for the bare ITO. It is obvious that the morphology of the thin layer of the PBI-1 aggregates on ITO seriously affects the work function of the electrode, likely due to the molecular orientation on the surface or the degree of order inside molecular aggregates [39]. The decreased work functions for both cases make it possible to use the PBI-1 modified ITO as the cathodes in the inverted OPVs, as explained below.

In optoelectronic devices, interfaces can significantly affect the energy level alignment of organic semiconductors and electrodes, which leads to important influences on the device performance [40]. Based on our observations above, it is possible to tune the work function of the electrode by controlling the morphology so as to match the energy level well of the active layer in device. Herein, the energy level alignment of the composite electrode with different surface morphologies and $C_{60}$ interface was measured via *in situ* UPS experiments, to establish the correlation between the electrode morphology and the interface properties. Fig. 3 shows the evolution of He UPS spectra with the increased thickness of $C_{60}$ on the PBI-1 modified ITO electrodes. For both the PBI-1 nanofibers and nanoparticles modified ITO electrodes, there are no peak signal observed in the corresponding valence band region near the Fermi level (blue lines in Fig. 3a and 3b right column), indicating the formation of composite electrode of ITO/PBI-1 aggregates due to the ultrathin layer
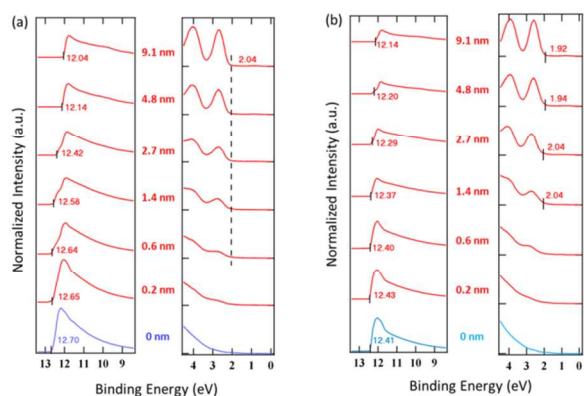
Figure 3. UPS spectra of binding energy regions (Left: secondary electron cutoff) and (Right: the valence band region) near the Fermi level of PBI-1 aggregates modified ITO (blue lines) and the sequential deposition of $C_{60}$ on PBI-1 aggregates with the thickness of $C_{60}$ indicated in between (red lines). (a) $C_{60}$ was deposited onto PBI nanofibers on ITO. (b) $C_{60}$ was deposited onto PBI-1 nanoparticles on ITO.

of PBI-1. The intensity of valence band for $C_{60}$ is still weak when the thickness of $C_{60}$ is less than 1 nm for both cases. Further increase in the $C_{60}$ thickness from 1.4 nm onward, nearly no shifts of the highest occupied molecular orbital (HOMO) leading edge was observed for ITO/PBI-1 nanofibers/$C_{60}$ as shown in Fig. 3a, with the HOMO leading edge at 2.04 eV below the Fermi level; while for ITO/PBI-1 nanoparticles/$C_{60}$ there is a small shift of 0.12 eV (from 2.04 eV to 1.92 eV). The minor difference between valance bands of $C_{60}$ in two systems could be attributed to the distribution of different domain facets and surface roughness of the polycrystalline $C_{60}$ films [38], likely induced by the microtopography of the PBI-1 aggregates. At the same time, as shown in Fig. 3a (left column), a big downward vacuum level shift of 0.66 eV (from 12.70 eV to 12.04 eV) can be found at the interface of $C_{60}$ and the composite electrode of ITO/PBI-1 nanofibers after the deposition of 9.1 nm $C_{60}$, which indicates a very strong charge transfer occurs at this interface. While for the interface between $C_{60}$ and ITO/PBI-1 nanoparticles, the vacuum level shift is only 0.27 eV (from 12.41 eV to 12.14 eV), indicating a relatively weaker charge transfer.
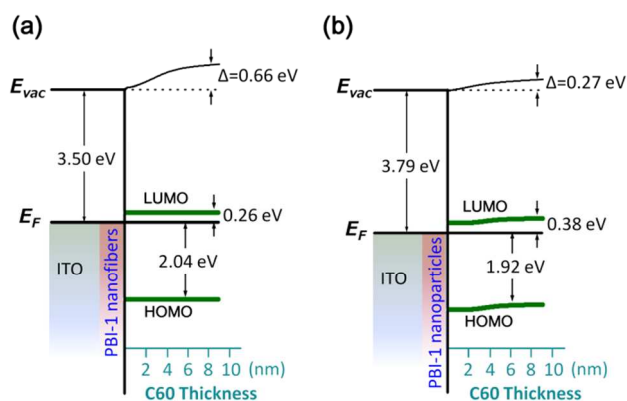


Figure 4. Energy level diagrams of the interfaces between $C_{60}$ and the composite electrodes of (a) ITO/PBI-1 nanofibers and (b) ITO/PBI-1 nanoparticles. $E_{VAC}$ and $E_F$ indicate the vacuum energy level and Fermi level, respectively.
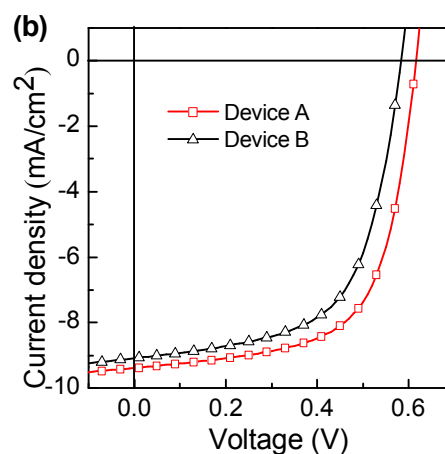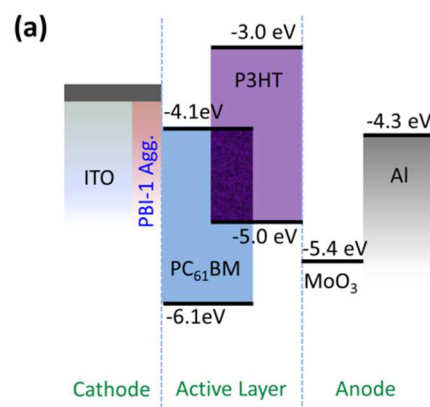


Figure 5. (a) Schematic illustration of the inverted device structure of ITO/PBI-1 aggregates (10 nm)/P3HT:PC$_{61}$BM (200 nm)/MoO$_3$ (10 nm)/Al (100 nm) with energy level alignments. (b) The curves of current density versus voltage for the inverted devices. PBI-1 nanofibers and nanoparticles were applied as the cathode interlayers in Device A (W$_F$: -3.50 eV) and Device B (W$_F$: -3.79 eV), respectively. The measurements were performed under 1000 W/m$^2$ air mass 1.5 global (AM 1.5 G) illumination.

The schematics of the energy level diagrams at the interfaces of $C_{60}$ and composite electrodes of ITO/PBI-1 aggregates are displayed in Fig. 4, in which the lowest unoccupied molecular orbital (LUMO) position of $C_{60}$ was calculated from HOMO-LUMO energy gap [41, 42]. The charge transfer property at the interfaces of the composite electrodes and $C_{60}$ layer could be related to the alignment of energy levels between them and the various surface morphologies of the electrodes. Since the interface charge transfer property directly affects the electron transition process, it is vital to optimize the device fabrication through controlling interlayer morphology.

Herein, motivated by this favourable decrease of the ITO work function and different charge transfer properties between $C_{60}$ and the composite electrode by the modification with PBI-1 aggregates, we applied the two kinds of composite electrodes as cathodes to construct inverted polymer solar cells with device structure of ITO/PBI-1 aggregates(10 nm)/rr-P3HT:PC$_{61}$BM(200 nm)/MoO$_3$(10 nm)/Al(100 nm), where rr-P3HT is the electron donating polymer, namely poly(3-hexylthiophene) and PC$_{61}$BM ([6,6]-phenyl C$_{61}$-butyric acid methyl ester) is the electron accepting material and MoO$_3$/Al acts as the anode (Fig. 5a). The current density-voltage (J-V) characteristics of the

inverted cells under AM1.5 G irradiation at 1000 W/m$^2$ are illustrated in the Fig. 5b, and comparison of the device (inverted) performance with different composite electrodes is given in the Table 1. As compared with Device B (PBI-1 nanoparticles as cathode interlayer), Device A (PBI-1 nanofibers as cathode interlayer) showed improvement in all the device parameters: open circuit voltage ($V_{OC}$) (0.58 V to 0.62 V), short circuit current ($J_{SC}$) (9.08 mA/cm$^2$ to 9.37 mA/cm$^2$) and fill factor (FF) (60.1% to 63.6%). As a result, the power conversion efficiency (PCE) of the Device A reached 3.69%, which is nearly 15% higher than the Device B. The enhanced device performance of Device A can be ascribed to the lower work function of the composite cathode (ITO/PBI-1 nanofibers), which shows easier extraction of electrons from the active layer. This is supported by the favoured electron transfer from the C$_{60}$ as observed by the *in situ* UPS measurements. In addition, PBI-1 nanofibers possess ordered molecular stacking compared with that of the nanoparticles, which allows faster electron transport from the active layer to the cathode. That means the series resistance of the device may decrease, resulting in the increased J$_{SC}$ and FF.

## Conclusions

We have studied the influence of the interlayer morphology by the surface work function, charge transfer between C$_{60}$ and the composite electrode, and the device performance of the inverted OPVs. PBI-1 nanofibers possess ordered molecular aggregation in contrast to the nanoparticles, which lowers the work function of ITO by 1 eV. The electron transfer from C$_{60}$ to the nanofibers modified ITO electrode is much preferred due to the relatively lower work function of the composite electrode. The inverted photovoltaic device using PBI-1 nanofibers as the cathode interlayer showed much better device performance, attributed to the increased electron extraction and transport properties of the interlayer. The results indicate that it is vital to optimize the morphology of the cathode interlayer in the device fabrication process to achieve higher PCE for inverted OPVs.

## Acknowledgements

## Notes and references

$^a$ Institute of Polymer Optoelectronic Materials and Devices, State Key Laboratory of Luminescent Materials and Devices, South China University of Technology, Guangzhou 510640, P. R. China.
E-mail: msxiez@scut.edu.cn
$^b$ Department of Chemistry, National University of Singapore, 3 Science Drive 3, 117543, Singapore.
E-mail: phycw@nus.edu.sg.
$^c$ State Key Laboratory of Supramolecular Structure and Materials, Jilin University, Qianjin Avenue, Changchun 130012, P. R. China.

1 W. L. Ma, C. Y. Yang, X. Gong, K. H. Lee and A. J. Heeger, *Adv. Funct. Mater.* 2005, **15**, 1617-1622.

2 G. Li, V. Shrotriya, J. S. Huang, Y. Yao, T. Moriarty, K. Emery and Y. Yang, *Nat. Mater.* 2005, **4**, 864-868.

3 S. Gune, H. Neugebauer and N. S. Sariciftci, *Chem. Rev.* 2007, **107**, 1324-1338.

4 C. J. Brabec, N. S. Saricftci and J. C. Hummelen, *Adv. Funct. Mater.* 2001, **1**, 15-26.

5 T. Minami, Semicond. *Sci. Tech.* 2005, **20**, S35-S44.

6 H. Kim, C. M. Gilmore, A. Pique, J. S. Horwitz, H. Mattoussi, H. Murata, Z. H. Kafafi and D. B. Chrisey, *J. Appl. Phys.* 1999, **86**, 6451-6461.

7 Y. Cao, G. Yu, C. Zhang, R. Menon and A. J. Heeger, *Synth. Met.* 1997, **87**, 171-174.

8 T. M. Brown, J. S. Kim, R. H. Friend, F. Cacialli, R. Daik and W. J. Feast, *Appl. Phys. Lett.* 1999, **75**, 1679-1681.

9 B. H. Zhang, W. M. Li, J. W. Yang, Y. Y. Fu, Z. Y. Xie, S. B. Zhang and L. X. Wang, *J. Phys. Chem. C* 2009, **113**, 7898-7903.

10 P. Tehrani, A. Kanciurzewska, X. Crispin, N. D. Robinson, M. Fahlman and M. Berggren, *Solid State Ionics* 2007, **177**, 3521-3527.

11 S. Wu, S. H. Han, Y. N. Zheng, H. Zheng, N. L. Liu, L. Wang, Y. Cao and J. Wang, *Org. Electron.* 2011, **12**, 504-508.

12 C. K. Mai, H. Q. Zhou, Y. Zhang, Z. B. Henson, T. Q. Nguyen, A. J. Heeger and G. C. Bazan, *Angew. Chem. Int. Ed.* 2013, **52**, 12874-12878.

13 C. K. Mai, R. A. Schlitz, G. M. Su, D. Spitzer, X. J. Wang, S. L. Fronkm, D. G. Cahill, M. L. Chabinyc and G. C. Bazan, *J. Am. Chem. Soc.* 2014, **136**, 13478-13481.

14 H. Q. Zhou, Y. Zhang, C. K. Mai, S. D. Collins, T. Q. Nguyen, G. C. Bazan and A. J. Heeger, *Adv. Mater.* 2014, **26**, 780-785.

15 H. Q. Zhou, Y. Zhang, C. K. Mai, J. Seifter, T. Q. Nguyen, G. C. Bazan and A. J. Heeger, *ACS Nano* 2015, **9**, 371-377.

16 H. Ishii, K. Sugiyama, E. Ito and K. Seki, *Adv. Mater.* 1999, **11**, 605-625.

17 Z. C. He, C. M. Zhong, S. J. Su, M. Xu, H. B. Wu and Y. Cao, *Nat. Photonics* 2012, **6**, 591-595.

18 M. Jørgensen, K. Norrman, S. A. Gevorgyan, T. Tromholt, B. Andreasen and F. C. Krebs, *Adv. Mater.* 2012, **24**, 580-612.

19 F. Huang, H. B. Wu and Y. Cao, *Chem. Soc. Rev.* 2010, **39**, 2500-2521.

20 Y. H. Zhou, C. F. Hernandez, J. Shim, J. Meyer, A. J. Giordano, H. Li, P. Winget, T. Papadopoulos, H. Cheun, J. Kim, M. Fenoll, A. Dindar, W. Haske, E. Najafabadi, T. M. Khan, H. Sojoudi, S. Barlow, S. Graham, J. L. Brédas, S. R. Marder, A. Kahn and B. Kippelen, *Science* 2012, **336**, 327-332.

21 R. M. Nie, A. Y. Li and X. Y. Deng, *J. Mate. Chem. A* 2014, **2**, 6734-6739.

22 A. Y. Li, R. M. Nie, X. Y. Deng, H. X. Wei, S. Z. Zheng, Y. Q. Li, J. X. Tang and K. Y. Wong, *Appl. Phys. Lett.* 2014, **104**, 123303-1-123303-4.

23 X. Y. Deng, R. M. Nie, A. Y. Li, H. X. Wei, S. Z. Zheng, W. B. Huang, Y. Q. Mo, Y. R. Su, Q. K. Wang, Y. Q. Li, J. X. Tang, J. B.

Xu and K. Y. Wong, *Adv. Mater. Interfaces* 2014, **1,** 1400215-1-1400215-6.

24 K. Sun, B. M. Zhao, A. Kumar, K. Y. Zeng and J. Y. Ouyang, *ACS Appl. Mater. Interfaces* 2012, **4**, 2009-2017.

25 S. J. Liu, K. Zhang, J. M. Lu, J. Zhang, H. L. Yip, F. Huang and Y. Cao, *J. Am. Chem. Soc.* 2013, **135**, 15326-15329.

26 Z. G. Zhang, B. Y. Qi, Z. W. Jin, D. Chi, Z. Qi, Y. F. Li and J. Z. Wang, *Energ. Environ. Sci.* 2014, **7**, 1966-1973.

27 F. Würthner, *Chem. Commun.* 2004, 1564-1579.

28 M. R. Wasielewski, *Acc. Chem. Res.* 2009, **42**, 1910-1921.

29 T. Seki, X. Lin and S. Yagai, *Asian J. Org. Chem.* 2013, **2**, 708-724.

30 A. W. Hains, H. Y. Chen, T. H. Reilly III and B. A. Gregg, *ACS Appl. Mater. Interfaces* 2011, **3**, 4381-4387.

31 T. Feng, B. Xiao, Y. Lv, Z. Q. Xie, H. B. Wu and Y. G. Ma, *Chem. Commun.* 2013, **49**, 6283-6285.

32 S. Braun, W. R. Salaneck and M. Fahlman, *Adv. Mater.* 2009, **21**, 1450-1472.

33 T. Yokoyama, S. Yokoyama, T. Kamikado, Y. Okuno and S. Mashiko, *Nature* 2001, **413**, 619-621.

34 Z. Q. Xie, V. Stepanenko, B. Fimmel and F. Würthner, *Mater. Horiz.* 2014, **1**, 355-359.

35 T. E. Kaiser, V. Stepanenko and F. Würthner, *J. Am. Chem. Soc.* 2009, **131**, 6719-6732.

36 S. Zhong, J. Q. Zhong, H. Y. Mao, J. L. Zhang, J. D. Lin and W. Chen, *Phys. Chem. Chem. Phys.* 2014, **14**, 14127-14141.

37 S. Zhong, J. Q. Zhong, H. Y. Mao, R. Wang, Y. Wang, D. C. Qi, K. P. Loh, A. T. S. Wee, Z. K. Chen and W. Chen, *ACS Appl. Mater. Interfaces.* 2012, **4**, 3134-3140.

38 S. Zhong, J. Q. Zhong, X. Z. Wang, M. Y. Huang, D. C. Qi, Z. K. Chen and W. Chen, *J. Phys. Chem. C* 2012, **116**, 2521-2526.

39 S. R. Day, R. A Hatton, M. A. Chesters and M. R. Willis, *Thin Solid Films* 2002, **410**, 159-166.

40 P. J. Hotchkiss, S. C. Jones, S. A. Paniagua, A. Sharma, B. Kippelen, N. R. Armstrong and S. R. Marder, *Acc. Chem. Res.* 2012, **45**, 337-346.

41 J. Hwang, A. Wan and A. Kahn, *Mater. Sci. Eng., R.* 2009, **64**, 1-31.

42 Y. L. Gao, *Mater. Sci. Eng., R.* 2010, **68**, 39-87.